



3D Numerical Simulation of Elastic Wave Propagation in Discrete Fracture Network Rocks

GUIWU CHEN,¹ LEI SONG,¹ and LANBO LIU²

Abstract—Fractures play an important role in controlling rock block stability and the hydraulic properties of fractured rock formations. Understanding elastic wave propagation in fractured media can result in significant advances for the geophysical prediction of fracture parameters from seismic data. However, most natural fracture characteristics, such as fracture length, aperture, angle and location are random; therefore, fracture models must be built discretely and follow some stochastic principles. We construct stochastic models of fractured rock samples using a random fracture network rather than a single fracture. Three-dimensional (3D) wave field computation is a computationally complex problem. Here, the 3D fourth-order in space, second-order in time, displacement-stress staggered-grid finite-difference scheme is used for accurate simulations. Our numerical examples demonstrate the effects of varying fracture number, aperture, and length distribution of the fracture network on the seismic response. The wave field scattering caused by the contrast between fractures and background media is one of the key features, and the resulting scattering is more obvious for S-waves than for P-waves. Such an approach can be applied to any fracture network model that provides a link between fracture parameters and seismic attributes.

Key words: Wave propagation, discrete fracture network, scattering, fracture parameter.

1. Introduction

Fractures have a significant effect on material strength (Morasch et al. 2015), rock block stability (Li et al. 2016), and fluid flow (Wu et al. 2018). In the oil and gas industry, understanding fractures for characterizing reservoir parameters and planning well-drilling is vital (Li et al. 2017). It is also

important in civil engineering and coal mining where proper support systems in tunnels and other underground structures are designed to accommodate fractures (Adewole and Bull 2013; Guo et al. 2019; Monsalve et al. 2019). Fractures can often jeopardize structural durability since aggressive substances (liquid solutions, ions and gases) may be able to penetrate and deteriorate a fractured material, leading in some cases to structural failure (Hilloulin et al. 2016). In such circumstances, fracture detection techniques have been a focus of attention (Chen and Zhang 2018; Osinowo et al. 2017). Chen and Zhang (2018) proposed a method to detect natural fractures from observed seismic data via inversion for fracture compliance. den Boer and Sayers (2018) present the underlying theory and implementation of a method for constructing a geologically realistic discrete fracture network, constrained by seismic amplitude variation with offset and azimuth data. Zhang et al. (2015) used the seismic signature to estimate the subsurface CO₂ flooded fracture properties. Most natural fracture networks do, however, exhibit some degree of spatial and geometric randomness of the single fracture, the impact of which on the seismic responses remains largely unexplored.

With the aim of estimating the fracture parameters of inaccessible structures, an understanding of seismic-wave propagation in fractured media is needed to explore how fracture heterogeneity can affect seismic properties. Physical experiments (e.g., Huang et al. 2016; Stewart et al. 2013) have been performed to test elastic properties in fractured rock samples. However, simulation in 3D is still necessary for a comprehensive understanding of seismic-wave responses across fractured media. Under the long-wavelength assumption (fracture size much smaller than the wavelength), wave propagation in such fractured media can be described in terms of effective

¹ State Key Laboratory of Geomechanics and Deep Underground Engineering, China University of Mining and Technology, Xuzhou 221116, China. E-mail: songlei@cumt.edu.cn

² Department of Civil and Environmental Engineering, University of Connecticut, 261 Glenbrook Road, Storrs, CT 06269-3037, USA.

anisotropic media. Various effective media models (e.g., Mavko et al. 2009; Saenger et al. 2006) are available for estimating the elastic parameters of fractured media. There has been significant progress in recent decades in seismic numerical modeling using stochastic fracture networks. Fang et al. (2017) generated a random fracture model with fracture spacing distribution following a power-law function, and then investigated the amplitude variation with offset (AVO) and Amplitude variation with azimuth (AVAz) responses of irregularly spaced fractures by comparing the numerical results obtained from an effective media model with a discrete fracture model, and found that the effective media assumption can result in a more than 10% error in fracture spacing inversion even though the fracture spacing ($< \lambda/20$) is much smaller than the seismic wavelength. Thus, scattered waves caused by strong heterogeneities can be modeled only by numerical simulation since a discrete random fracture network cannot be represented by any effective media theory. This is because the effective media theories consider the general properties of both fractures and host rock within the

study volume. Therefore, to obtain fully detailed seismic characteristics, a fracture network should be treated as a set of local inclusions. De Basabe et al. (2016) modeled elastic wave propagation in fractured media using the discontinuous Galerkin method. Hunziker et al. (2018) studied seismic attenuation and stiffness modulus dispersion in porous rocks containing stochastic fracture networks in 2D and then concluded that information about the local connectivity of a fracture network could be retrieved from seismic data.

The weak-inclusion scheme (Saenger and Bohlen 2004) describes fractures as low-velocity and low-density ellipsoidal inclusions. However, this scheme requires fine grid spacing to adequately model the thickness of fractures. The local effective-media scheme (Coates and Schoenberg 1995; Vlastos et al. 2003) expresses the effective compliance of a fractured layer with the sum of compliances from each fracture and the background media within each discretized cell. This results in local fractured media that has a lower velocity than the background media. Thus, this scheme requires a much larger grid spacing

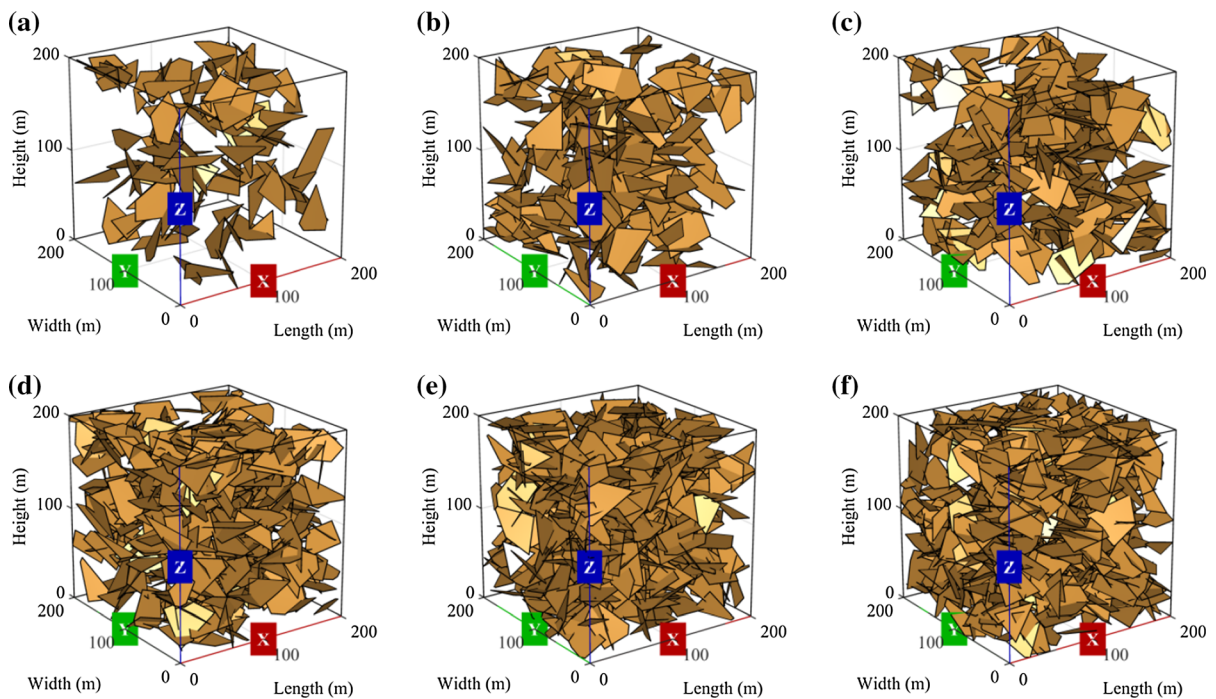


Figure 1

3D fracture networks with six different fracture numbers (from 100 to 600, increasing alphabetically)

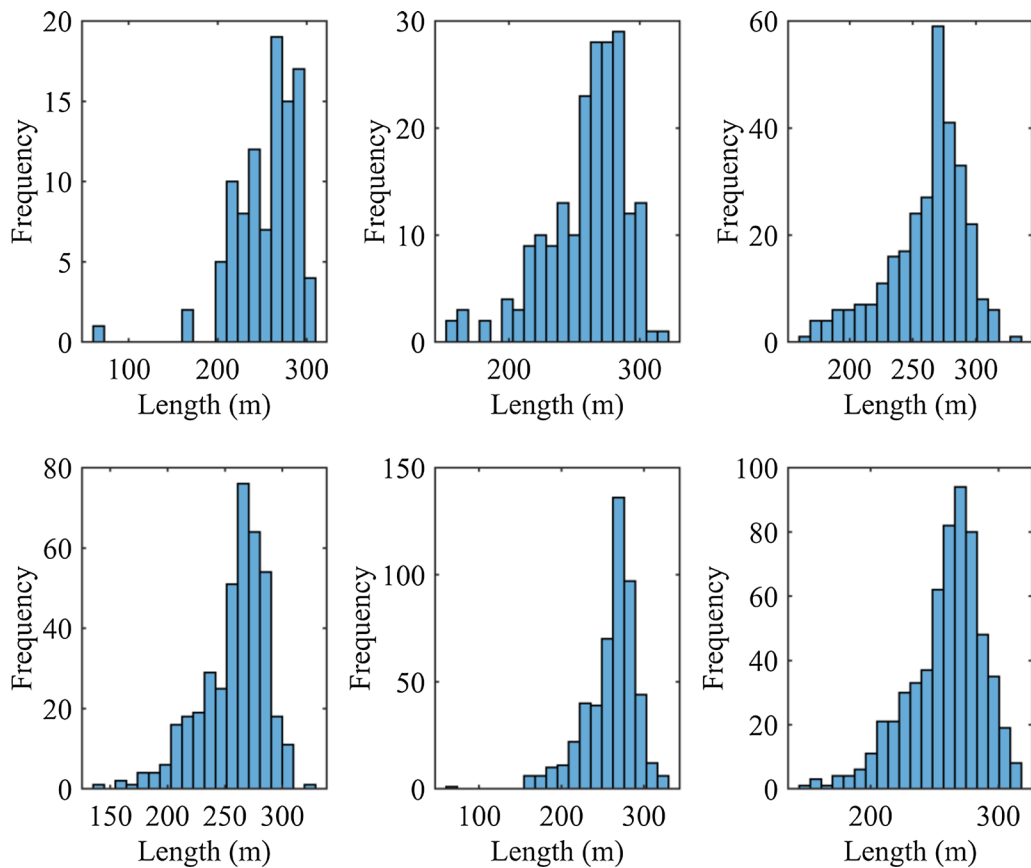


Figure 2
Fracture length distribution analysis applied to the fracture network shown in Fig. 1

than the weak-inclusion scheme. For simplicity and without loss of applicability, we focus in the following on the effect of stochastic properties on natural fracture networks, and directly use this scheme to compute an effective modulus for each of the voxels in the 3D image.

The goal of our paper is to investigate the seismic response and uncertainty quantification with such heterogeneities in randomly fractured media and subsequently to provide more reliable predictions for practical problems. Stochastic 3D fracture networks were used to represent natural fracture networks. We applied a staggered-grid finite-difference scheme to numerically study elastic wave propagation directly in voxelized 3D stochastic fracture geometries without meshing. Elastic parameters of the fracture and background media were assigned to each of the voxels in the 3D image. This approach can provide

detailed wave propagation phenomena resulting from the spatial contrasts between background and fractures.

2. Natural Fracture Model

Natural fracture systems can often be represented by a set of convex polygons in a probed volume, with random shapes, sizes and locations. Based on these assumptions, a fracture can be represented by a flat object, with its shape defined as a convex polygon (rectangle, ellipse or more complex form), and with its size following a known distribution function such as negative exponential (Cheng-Haw et al. 2006; Zazoun 2008). Similarly, its location is obtained by means of spatial functions such as a 3D Poisson or uniform distribution. The orientation information can

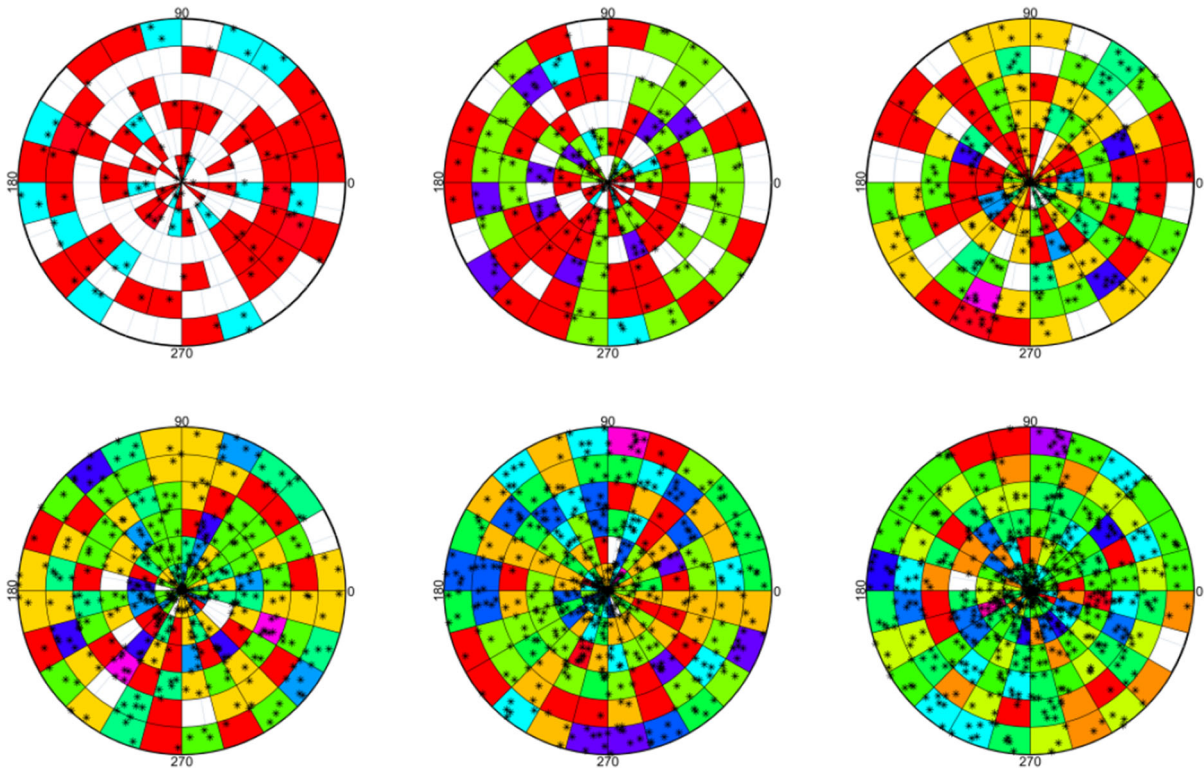


Figure 3
Orientation and dip angle distribution analysis applied to the fracture network shown in Fig. 1

be extracted uniformly. Then, every fracture can be built discretely following the rules above. In this paper, we simulate 3D fracture networks using the ADFNE package (Alghalandis 2017). For the simulation of a 3D fracture network containing n fractures, the following MATLAB function was used.

```
fnw = GenFNM3D(n, dip, ddip, ddir, dddir, s, rgn);
```

where *dip* and *ddip* denote the mean dip angle $[0, \pi/2)$ and the variation limit around the dip angle ($0 \leq ddir \leq \pi/4$), respectively. *ddir* is the mean orientation $[0, 2\pi)$ and *dddir* is variation limit around the *ddir* angle ($0 \leq dddir \leq \pi$) for fractures, *rgn* is the region of study $[x_{\min}, x_{\max}, y_{\min}, y_{\max}, z_{\min}, z_{\max}]$ (a cube) by which the simulated fracture network is clipped and *s* is the scaling factor to determine maximum size ($s = S_{\max}$) for generated fracture lengths, which is distributed according to a negative exponential distribution $l \sim \text{Exp}(\lambda)$.

The lengths of our random convex polygon fractures are drawn from the negative exponential described above, and the orientations of the fractures and the positions of the fracture centers are drawn from a uniform distribution.

The side length L , width W , and height H of the sample were all fixed at 1000 m. The maximum fracture length was set to be $l_{\max} = L/2 = 500$ m,

Table 1

Compressional-wave velocity (v_p), shear-wave velocity (v_s), and density (ρ) of the homogeneous media and the crack infills

Elasticity parameters	Background media (homogenous matrix)	Crack infill (cold water)
v_p (m/s ²)	6000.0	1477.2
v_s (m/s ²)	3454.0	0.0
ρ (kg/m ³)	2500.0	999.0

because having fractures larger than half the sample size would mechanically weaken the sample.

We vary the fracture number n from 100 to 600. To illustrate the diversity of the considered stochastic fracture networks, we show six examples in Fig. 1. For each example, the length distribution and orientation information are plotted in Figs. 2 and 3, respectively.

3. 3D Fourth-Order Finite-Difference Time-Domain Scheme

First, we present the displacement-stress equation for a 3D elastic wave in inhomogeneous, isotropic media

$$\begin{cases} \rho \frac{\partial^2 u_x}{\partial t^2} = \frac{\partial \tau_{xx}}{\partial x} + \frac{\partial \tau_{xy}}{\partial y} + \frac{\partial \tau_{xz}}{\partial z} \\ \rho \frac{\partial^2 u_y}{\partial t^2} = \frac{\partial \tau_{xy}}{\partial x} + \frac{\partial \tau_{yy}}{\partial y} + \frac{\partial \tau_{yz}}{\partial z} \\ \rho \frac{\partial^2 u_z}{\partial t^2} = \frac{\partial \tau_{xz}}{\partial x} + \frac{\partial \tau_{yz}}{\partial y} + \frac{\partial \tau_{zz}}{\partial z} \end{cases} \quad (1)$$

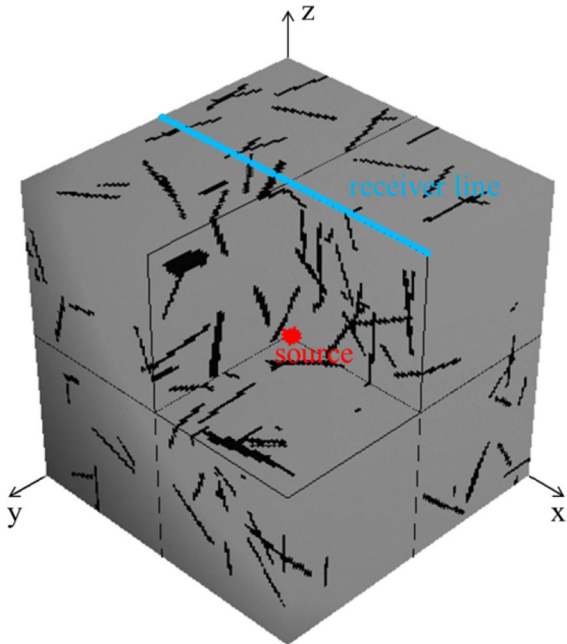


Figure 4

This is a sketch of the model setup in 3D. The background is homogeneous rock (gray) and the fractures (black) are randomly distributed in the sketch. The source (red symbol) is located in the central position of the model, and the receivers (light blue dots) are spread out in a line. The domain is 1 km in the x -, y - and z -directions

where ρ is ambient density, u_x , u_y and u_z represent the displacements of particle motion in the x , y and z directions, and x , y and z are the spatial coordinates. τ_{ij} is the stress tensor, $i, j \in \{x, y, z\}$.

Hooke's Law for a perfectly elastic, heterogeneous, isotropic media is

$$\begin{bmatrix} \tau_{xx} \\ \tau_{yy} \\ \tau_{zz} \\ \tau_{yz} \\ \tau_{xz} \\ \tau_{xy} \end{bmatrix} = \begin{bmatrix} \lambda + 2\mu & \lambda & \lambda & 0 & 0 & 0 \\ \lambda & \lambda + 2\mu & \lambda & 0 & 0 & 0 \\ \lambda & \lambda & \lambda + 2\mu & 0 & 0 & 0 \\ 0 & 0 & 0 & \mu & 0 & 0 \\ 0 & 0 & 0 & 0 & \mu & 0 \\ 0 & 0 & 0 & 0 & 0 & \mu \end{bmatrix} \begin{bmatrix} e_{xx} \\ e_{yy} \\ e_{zz} \\ e_{yz} \\ e_{xz} \\ e_{xy} \end{bmatrix} \quad (2)$$

where e_{ij} is the strain tensor, $i, j \in \{x, y, z\}$, λ is the Lamé elastic coefficient, and μ is the shear modulus.

The displacement-strain formulation is defined as follows:

$$\begin{cases} e_{xx} = \frac{\partial u_x}{\partial x} \\ e_{yy} = \frac{\partial u_y}{\partial y} \\ e_{zz} = \frac{\partial u_z}{\partial z} \\ e_{yz} = \frac{\partial u_z}{\partial y} + \frac{\partial u_y}{\partial z} \\ e_{xz} = \frac{\partial u_z}{\partial x} + \frac{\partial u_x}{\partial z} \\ e_{xy} = \frac{\partial u_y}{\partial x} + \frac{\partial u_x}{\partial y} \end{cases} \quad (3)$$

The velocities of P- and S-waves in homogeneous, isotropic, elastic media are given by

$$v_p = \sqrt{\frac{K + 4\mu/3}{\rho}} = \sqrt{\frac{\lambda + 2\mu}{\rho}} \quad (4)$$

$$v_s = \sqrt{\frac{\mu}{\rho}} \quad (5)$$

where v_p is the P-wave velocity, v_s is the S-wave velocity, K is the bulk modulus.

To obtain a broader bandwidth result, we apply a fourth-order staggered-grid finite-difference scheme to approximate the temporal and spatial derivatives (Moczo 2000). The split perfectly matched layer (Li and Huang 2013) absorbing boundary condition is applied to eliminate reflections from the model boundaries.

To minimize numerical artifacts and avoid instabilities, we apply spatial and temporal sampling criteria modified after and (Moczo 2000):

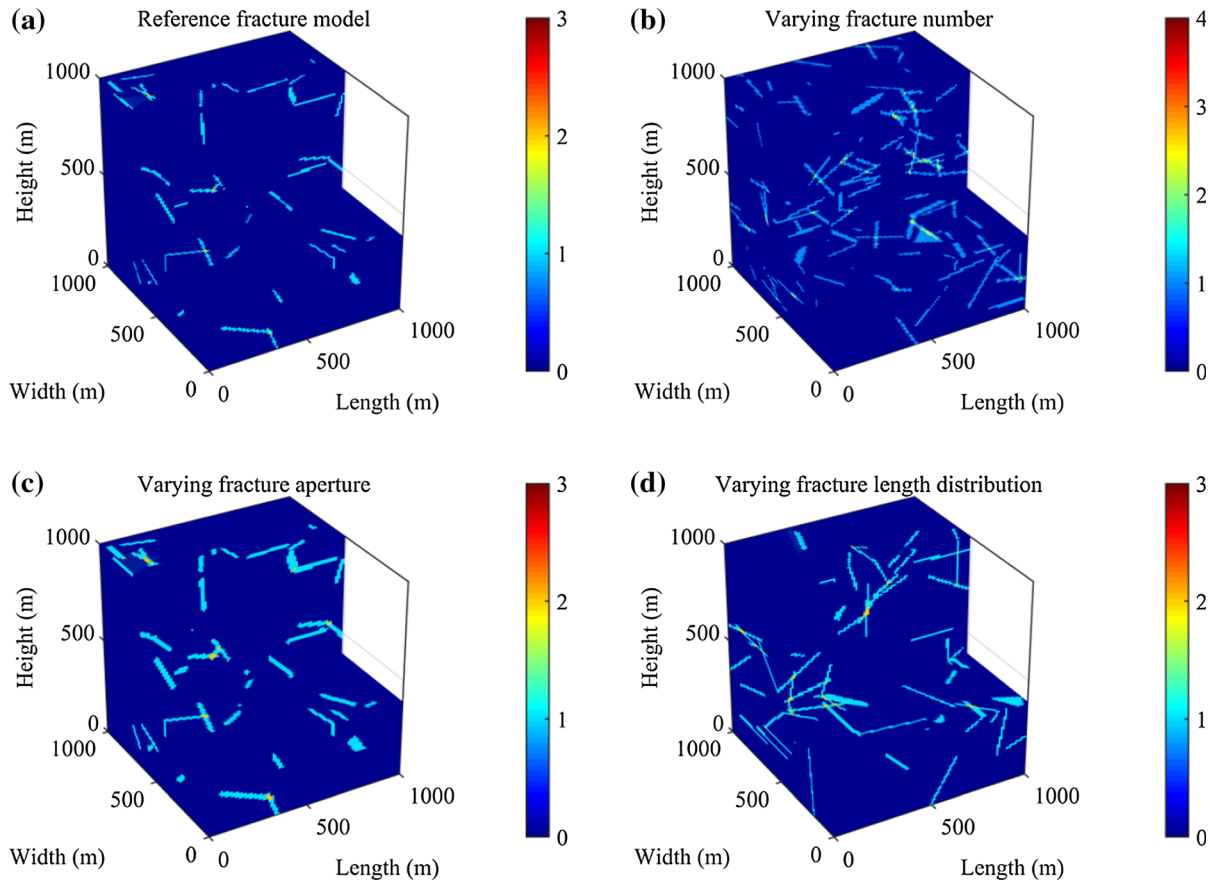


Figure 5

Four models used for modeling elastic wave propagation: **a** reference fracture model with equal apertures; fractures are represented by a stochastic fracture network. The fracture length is distributed according to a negative exponential distribution $l \sim E(\lambda)$ with mean $\lambda = 250$ m, an aperture of 1 m, and a fracture number of 100. **b** Fracture number is changed to 500. **c** Fracture aperture is changed to 2 m. **d** Fracture length distribution is changed according to a negative exponential distribution $l \sim E(\lambda)$ with mean $\lambda = 350$ m. Color bars indicate the number of connections in each grid

$$dt \leq \frac{6}{7\sqrt{3}} \frac{dh}{v_{\max}} \quad (6)$$

where v_{\max} is the largest elastic wave velocity, and dh is grid spacing, which is determined by the type and order of the finite-difference (FD) scheme.

For the full elastic wave field, the P-wave component is an irrotational field, and the S-wave component is non-dispersed. Following (Sun et al. 2004), P- and S-waves were separated.

4. Numerical Examples

To address the relationships between fracture parameters and elastic wave propagation, we conduct the following numerical experiments. The wave field was simulated in a $1000 \text{ m} \times 1000 \text{ m} \times 1000 \text{ m}$ homogeneous, isotropic, linear-elastic space containing a stochastic fracture network. The material properties used in the simulation are shown in

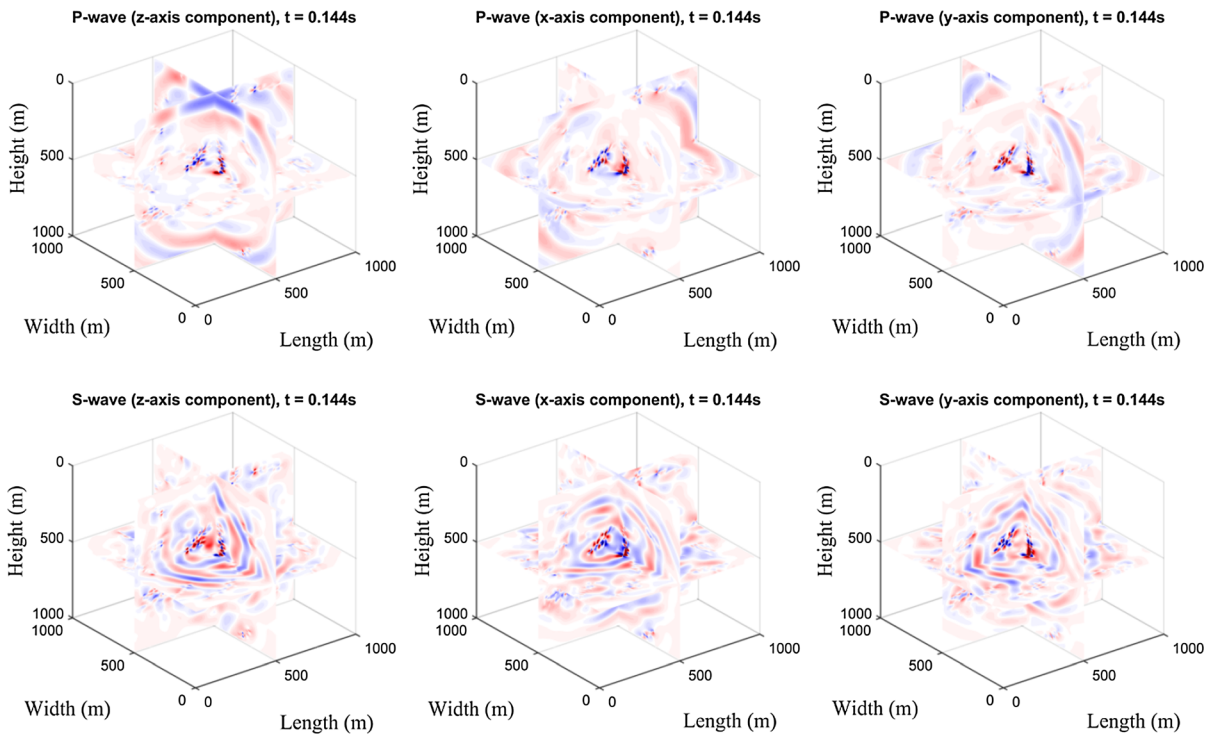


Figure 6

Snapshots of the 3D elastic wave field for each of the P- and S-wave components for a reference fracture model at 0.144 s. The scattering waves from the fracture can be clearly seen for each component

Table 1 (Kruger et al. 2007). Source location is (500, 500, 500 m), and a Ricker wavelet point source with a peak frequency of 20 Hz is used. The sketch of our models and source-receiver geometry is shown in Fig. 4. Our numerical model uses $100 \times 100 \times 100$ discretized grid points with an even spatial spacing of 10 m. The time step is 0.48 ms, and the numerical mesh is made up of cube grid cells. Models of inner structures and mesh details are shown in Fig. 5. We show results for three different scenarios: (1) fixed fracture number, aperture, and length distribution, (2) varying fracture number, fixed fracture aperture, and length distribution, (3) fixed fracture number and length distribution, but larger fracture aperture than scenario (1), and (4) varying fracture length distribution, fixed fracture number, and aperture.

In the reference fracture model, the fractures have an equal aperture (1 m), the fracture number is 100, and fracture lengths were extracted from a negative exponential distribution ($\lambda = 250$ m). Figure 6 shows snapshots of the 3D elastic wave field for each of the P- and S-wave components at 0.144 s. From the wave field snapshots, the scattering waves from the fracture can be seen clearly for each component. More significant scattering was found for S-waves than for P-waves, because the P-wave wave length is greater than the S-wave wave length. Figure 10 shows an elastic-wave multicomponent shot record for a reference fracture model. From the shot gathers, we found that more significant scattering occurred in the S-waves.

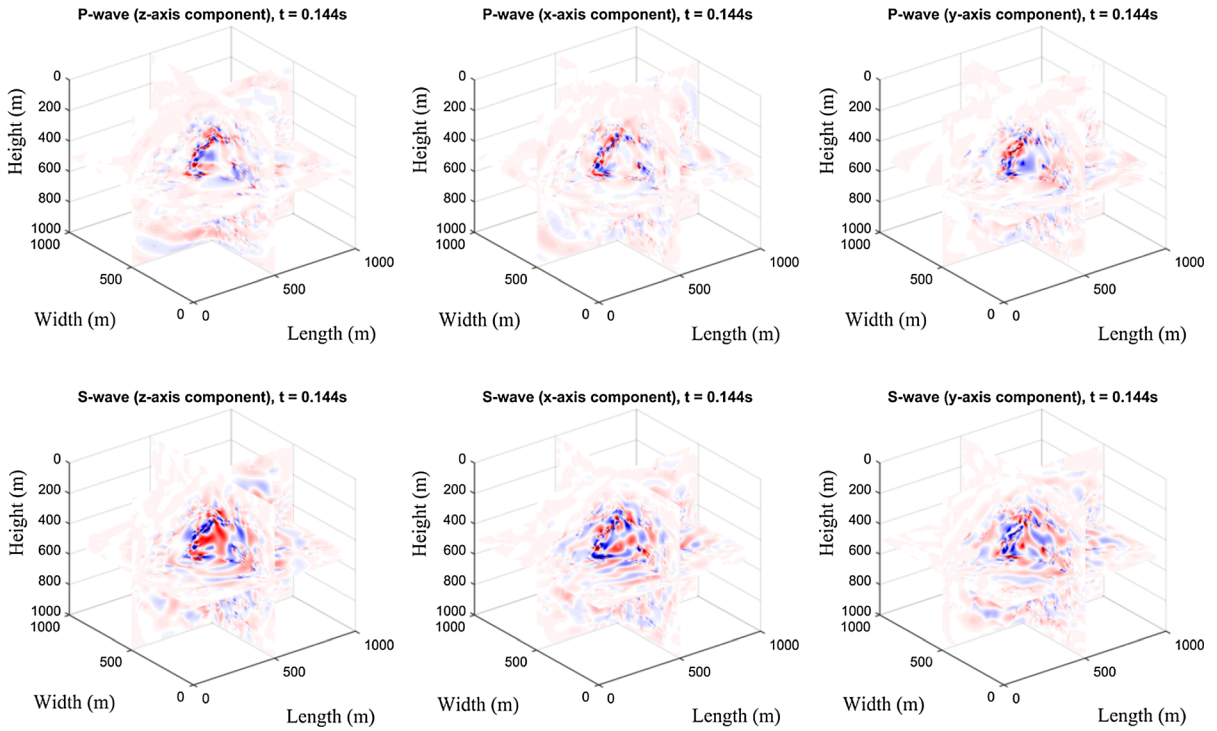


Figure 7

Snapshots of the 3D elastic wave field for each of the P- and S-wave components for a fracture model with a varying fracture number at 0.144 s

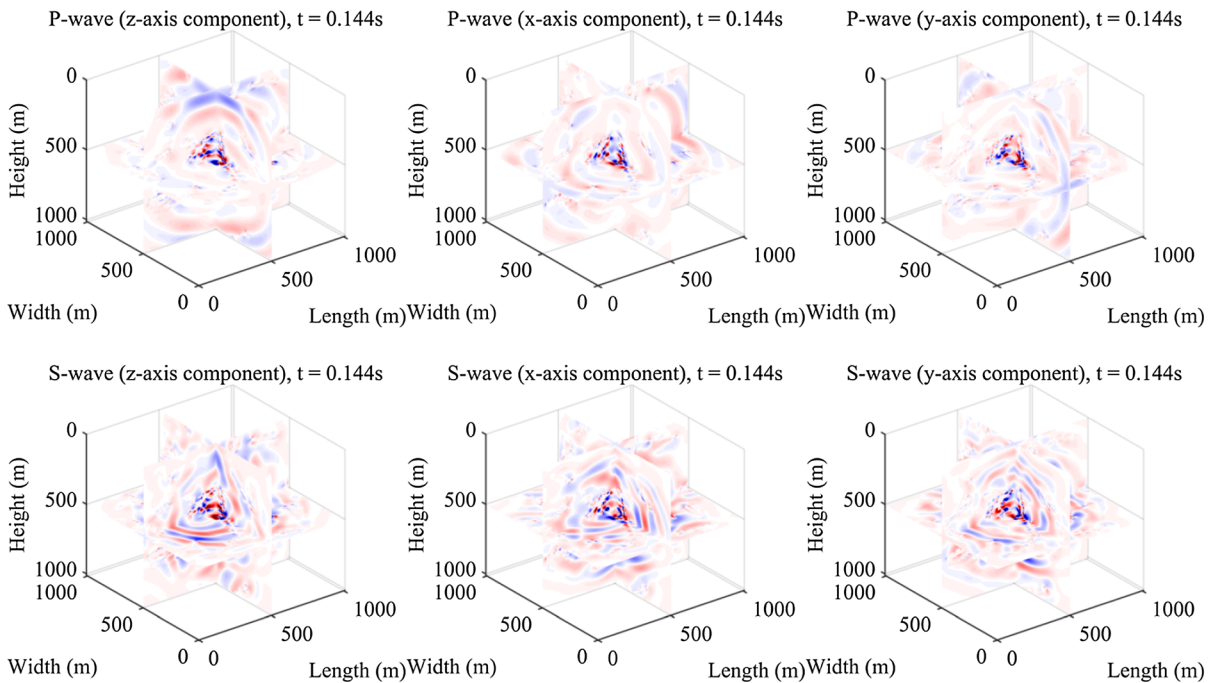


Figure 8

Three-dimensional slices of elastic-wave-field multicomponent snapshots of the displacement for a fracture model with a varying fracture aperture at 0.144 s

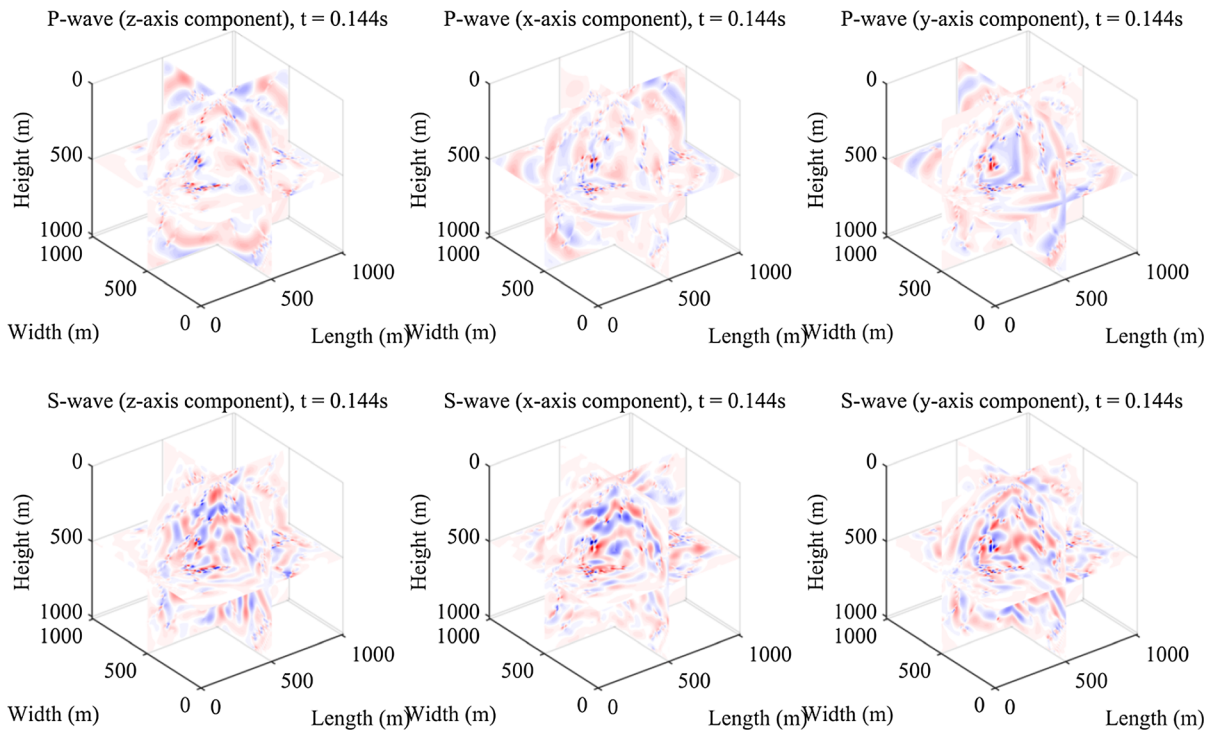


Figure 9

Snapshots of the 3D elastic wave field for each of the P- and S-wave components for a fracture model with a varying fracture length distribution at 0.144 s

By increasing the fracture number, the sources of scattering increased as well. This results in a distortion of the wave front. In the second model, the fracture number increases to 300. Figure 7 shows snapshots of the 3D elastic wave field for each of the P- and S-wave components for a fracture model with 300 fractures at 0.144 s. Figure 11 shows a corresponding shot record. As the fracture number increases, the wave field and shot records becomes more complex. This is caused by the increased number of scattering sources, which in turn increases the chances of having constructive or destructive interference from the transmitted waves.

In the third model, the fracture parameters are the same as in the reference model with the exception of the aperture. We changed the fracture aperture to 2 m. Figure 8 shows snapshots of the 3D elastic wave

field for each of the P- and S-wave components for a fracture model with varying fracture apertures at 0.144 s. Figure 12 shows a multicomponent shot record for this model. As the fracture aperture increases, the fracture volume in this region increases. With higher fracture volume, we have more significant phase shifts. Significant disturbance was identified by scattered waves passing through the individual fractures.

From the above results, we found that random fractures give us very complicated scattering patterns due to constructive and destructive interference. The variation in fracture number increased the chances of this interference and tended to result in complex scattering patterns, whereas the fracture aperture variation enhanced this interference leading to obvious scattering patterns. Therefore, we changed the

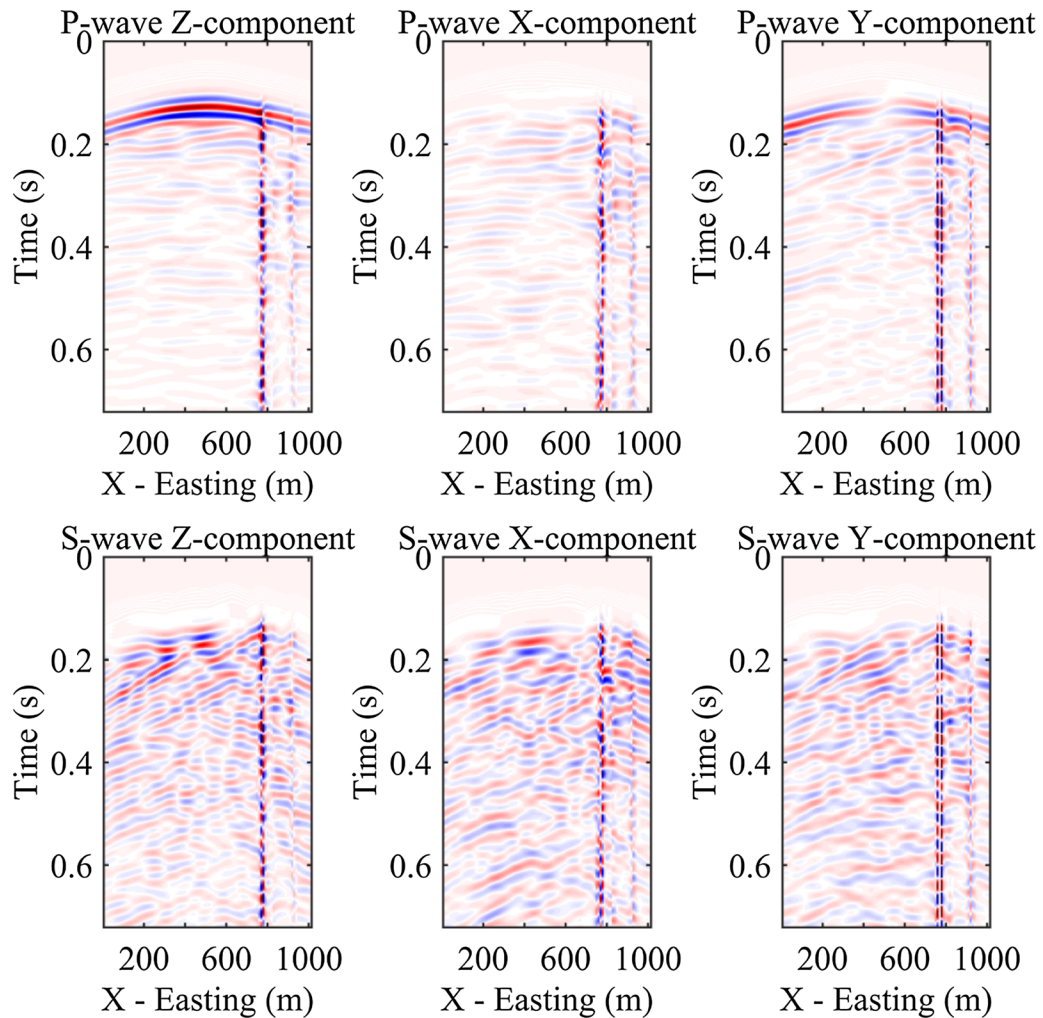


Figure 10
Elastic-wave multicomponent shot records for a reference fracture model

fracture length distribution. In the last model, fracture length is distributed according to a negative exponential distribution $l \sim E(\lambda)$ with mean $\lambda = 350$ m, fracture aperture of 1 m, and fracture number of 100. Figure 9 shows snapshots of the 3D elastic wave field for each of the P- and S-wave components for a fracture model with varying fracture apertures at 0.144 s. Figure 13 shows the corresponding

multicomponent shot record. As the fracture length increased, the scales of the scattering sources increased as well. Significant disturbance was observed as a result of the scattered wave passing through an individual fracture. This causes a reduction in wave interference, which in turn causes the “blurry” pattern observed in the wave field snapshots (Figs. 10, 11, 12, 13).

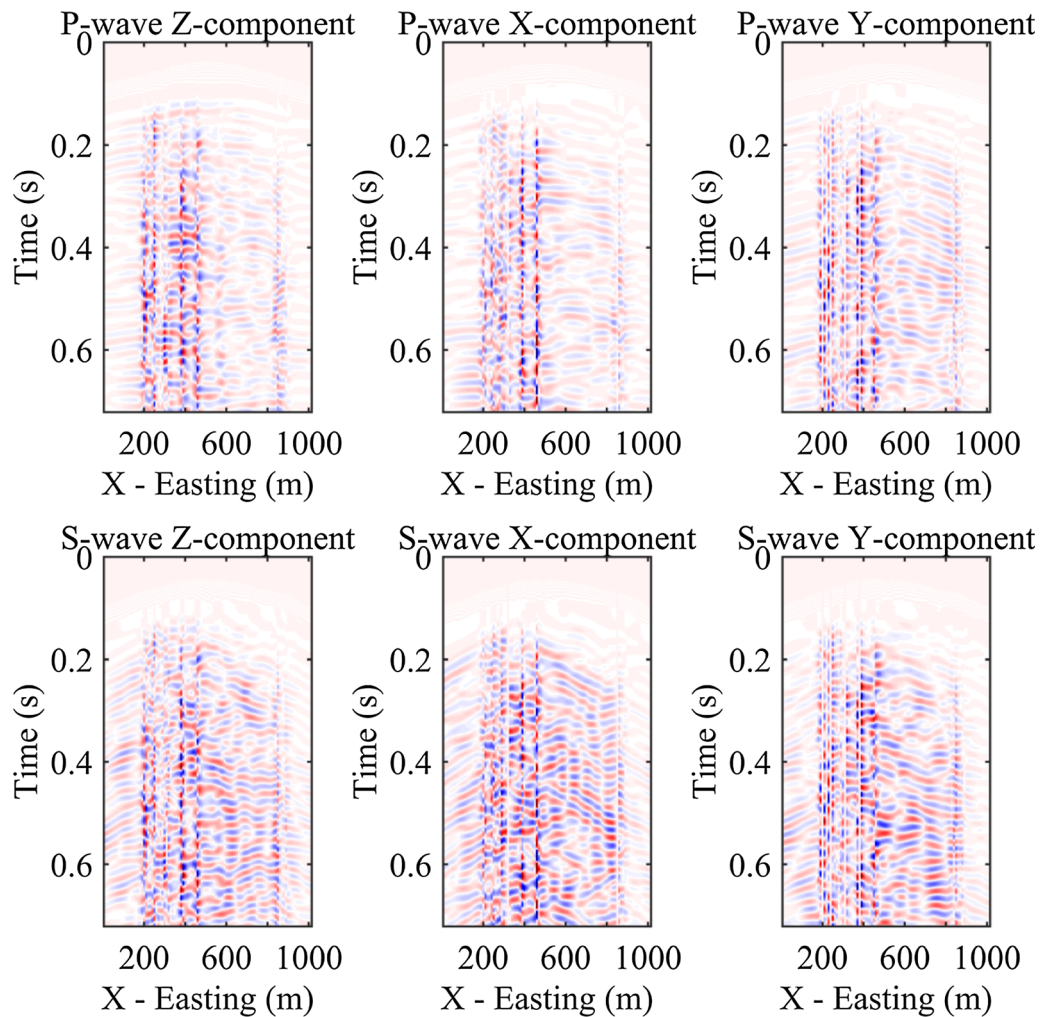


Figure 11
Elastic-wave multicomponent shot records for a fracture model with a varying fracture number

5. Conclusions

We have combined stochastic fracture network modeling and a staggered-grid finite-difference scheme to model elastic wave propagation in 3D fractured media. The considered fracture networks are isotropic convex polygons and the length for each fracture is obtained from a negative exponential (E) distribution. Orientation information and dip

angle were extracted from uniform and Fisher distributions, respectively. The wave field was calculated using the 3D fourth-order staggered-grid finite-difference method. We numerically acquired the elastic wave field for a fractured media. We compared wave fields based on changes to the fracture number, fracture aperture, and fracture length distribution of the fracture models. From the wave field snapshots, we found that random fractures can

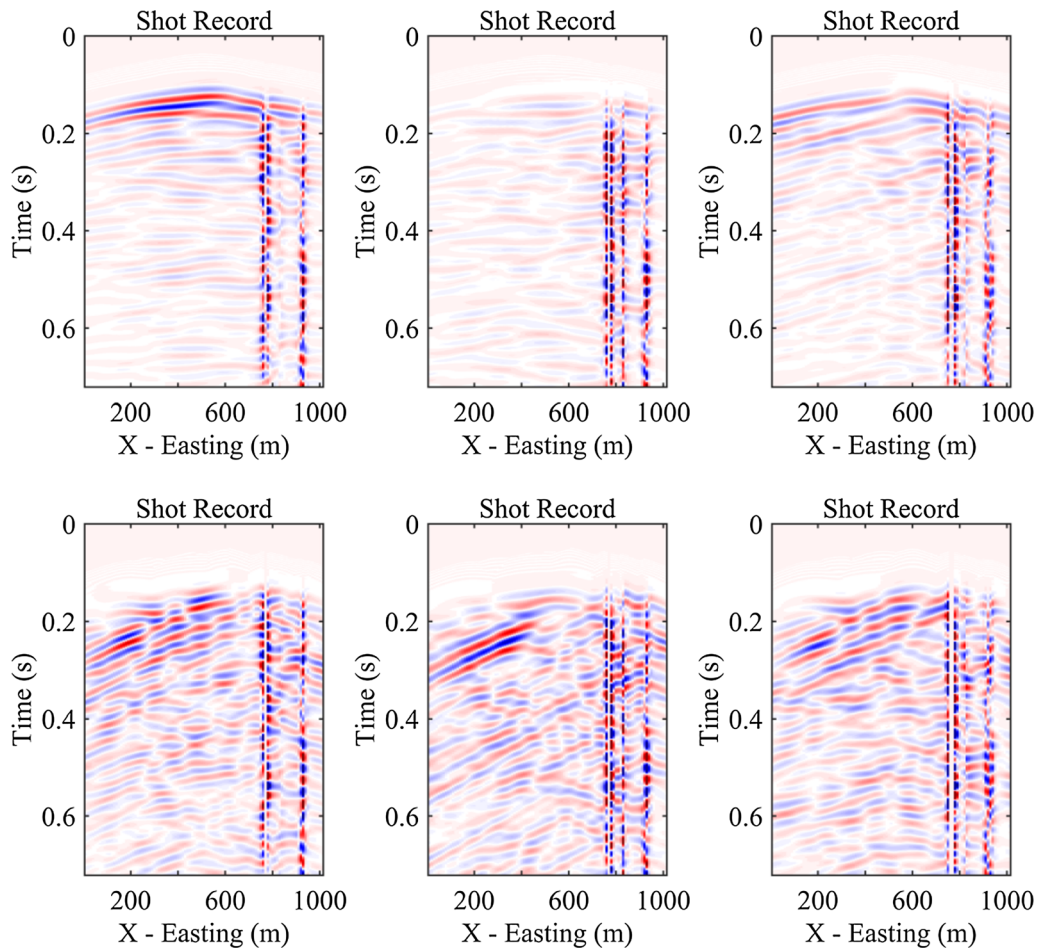


Figure 12
Elastic-wave multicomponent shot records for a fracture model with a varying fracture aperture

result in complicated scattering patterns due to constructive and destructive interference. As fracture numbers increased, the chances of this interference increased and complex scattering patterns were observed. In contrast, when variation in the fracture aperture was enhanced, the interference resulted in obvious scattering patterns. As the fracture length increased, the scales of scattered sources increased as well. Significant disturbance was observed as the result of a scattered wave passing through an individual fracture. This causes a reduction in wave interference, which in turn causes the “blurry”

pattern seen in the wave field snapshots. Furthermore, with the change of fracture parameters, the elastic modulus of fractured media changed. We conclude that elastic wave scattering is sensitive to the fracture parameters. Wave field scattering caused by the contrast between fractures and background media is one of the key features, and the resulting scattering is more complex for S-waves than for P-waves. Our numerical method can be used to explore seismic responses, such as AVO properties, attenuation and dispersion, on fracture parameters.

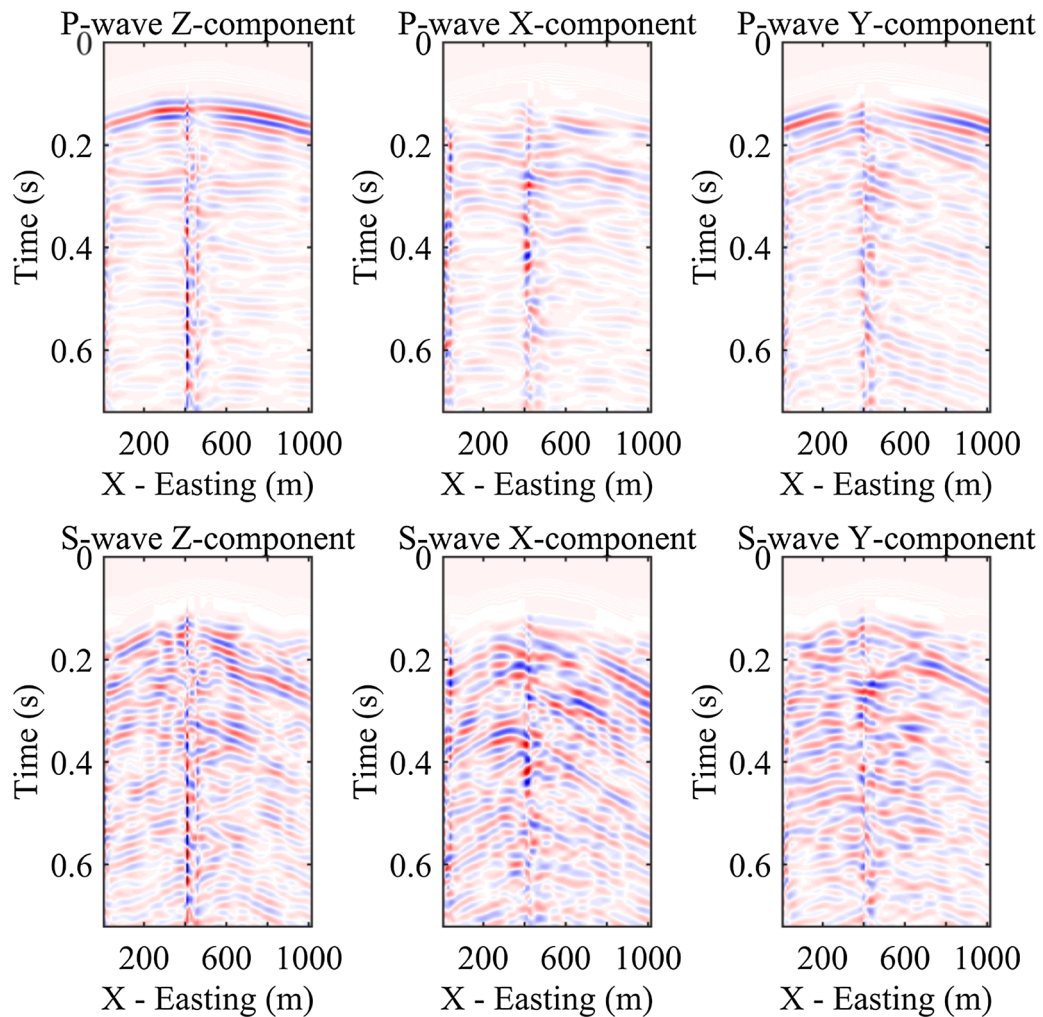


Figure 13

Elastic-wave multicomponent shot records for a fracture model with a varying fracture length distribution

Acknowledgements

This research is supported by “the Fundamental Research Funds for the Central Universities” (2018ZDPY08) and the National Science Foundation of China (NSFC grant no. 41474122). We would like to thank Dr. Younes Fadakar Alghalandis for providing ADFNE software for discrete fracture modeling.

Publisher’s Note Springer Nature remains neutral with regard to jurisdictional claims in published maps and institutional affiliations.

REFERENCES

- Adewole, K. K., & Bull, S. J. (2013). Prediction of the fracture performance of defect-free steel bars for civil engineering applications using finite element simulation. *Construction and Building Materials*, *41*, 9–14. <https://doi.org/10.1016/j.conbuildmat.2012.11.089>.
- Alghalandis, Y. F. (2017). ADFNE: open source software for discrete fracture network engineering, two and three dimensional applications. *Computers & Geosciences*, *102*, 1–11. <https://doi.org/10.1016/j.cageo.2017.02.002>.
- Chen, H., & Zhang, G. (2018). Detection of natural fractures from observed surface seismic data based on a linear-slip model. *Pure and Applied Geophysics*, *175*, 2769–2784. <https://doi.org/10.1007/s00024-018-1848-3>.

- Cheng-Haw, L., Chen-Chang, L., & Bih-Shan, L. (2006). The estimation of dispersion behavior in discrete fractured networks of andesite in Lan-Yu Island, Taiwan. *Environmental Geology*, 52, 1297–1306. <https://doi.org/10.1007/s00254-006-0568-7>.
- Coates, R. T., & Schoenberg, M. (1995). Finite-difference modeling of faults and fractures. *Geophysics*, 60, 1514–1526. <https://doi.org/10.1190/1.1443884>.
- De Basabe, J. D., Sen, M. K., & Wheeler, M. F. (2016). Elastic wave propagation in fractured media using the discontinuous Galerkin method. *Geophysics*, 81, T163–T174. <https://doi.org/10.1190/geo2015-0602.1>.
- den Boer, L. D., & Sayers, C. M. (2018). Constructing a discrete fracture network constrained by seismic inversion data. *Geophysical Prospecting*, 66, 124–140. <https://doi.org/10.1111/1365-2478.12527>.
- Fang, X., Zheng, Y., & Fehler, M. C. (2017). Fracture clustering effect on amplitude variation with offset and azimuth analyses. *Geophysics*, 82, N13–N25. <https://doi.org/10.1190/geo2016-0045.1>.
- Guo, W., Zhao, G., Lou, G., & Wang, S. (2019). Height of fractured zone inside overlying strata under high-intensity mining in China. *International Journal of Mining Science and Technology*, 29, 45–49. <https://doi.org/10.1016/j.ijmst.2018.11.012>.
- Hilloulin, B., et al. (2016). Monitoring of autogenous crack healing in cementitious materials by the nonlinear modulation of ultrasonic coda waves, 3D microscopy and X-ray microtomography. *Construction and Building Materials*, 123, 143–152. <https://doi.org/10.1016/j.conbuildmat.2016.06.138>.
- Huang, L., Stewart, R. R., Dyaour, N., & Baez-Franceschi, J. (2016). 3D-printed rock models: Elastic properties and the effects of penny-shaped inclusions with fluid substitution. *Geophysics*, 81, D669–D677. <https://doi.org/10.1190/geo2015-0655.1>.
- Hunziker, J., Favino, M., Caspari, E., Quintal, B., Rubino, J. G., Krause, R., et al. (2018). Seismic attenuation and stiffness modulus dispersion in porous rocks containing stochastic fracture networks. *Journal of Geophysical Research: Solid Earth*, 123, 125–143. <https://doi.org/10.1002/2017jb014566>.
- Kruger, O. S., Saenger, E. H., Oates, S. J., & Shapiro, S. A. (2007). A numerical study on reflection coefficients of fractured media. *Geophysics*, 72, D61–D67. <https://doi.org/10.1190/1.2732690>.
- Li, X., Dao, M., Eberl, C., Hodge, A. M., & Gao, H. (2016). Fracture, fatigue, and creep of nanotwinned metals. *MRS Bulletin*, 41, 298–304. <https://doi.org/10.1557/mrs.2016.65>.
- Li, J., & Huang, Y. (2013). *Time-domain finite element methods for Maxwell's equations in metamaterials.*, Springer series in computational mathematics New York: Springer. <https://doi.org/10.1007/978-3-642-33789-5>.
- Li, H., Lu, Y., Zhou, L., Tang, J., Han, S., & Ao, X. (2017). Experimental and model studies on loading path-dependent and nonlinear gas flow behavior in shale fractures. *Rock Mechanics and Rock Engineering*, 51, 227–242. <https://doi.org/10.1007/s00603-017-1296-x>.
- Mavko, G., Mukerji, T., & Dvorkin, J. (2009). *The rock physics handbook* (2nd ed.). Cambridge: Cambridge University Press.
- Moczo, P. (2000). 3D fourth-order staggered-grid finite-difference schemes: Stability and grid dispersion. *Bulletin of the Seismological Society of America*, 90, 587–603. <https://doi.org/10.1785/0119990119>.
- Monsalve, J. J., Baggett, J., Bishop, R., & Ripepi, N. (2019). Application of laser scanning for rock mass characterization and discrete fracture network generation in an underground limestone mine. *International Journal of Mining Science and Technology*, 29, 131–137. <https://doi.org/10.1016/j.ijmst.2018.11.009>.
- Morasch, A., Reeb, A., Baier, H., Weidenmann, K. A., & Schulze, V. (2015). Characterization of debonding strength in steel-wire-reinforced aluminum and its influence on material fracture. *Engineering Fracture Mechanics*, 141, 242–259. <https://doi.org/10.1016/j.engfracmech.2015.05.029>.
- Osinowo, O. O., Chapman, M., Bell, R., & Lynn, H. B. (2017). Modelling orthorhombic anisotropic effects for reservoir fracture characterization of a naturally fractured tight carbonate reservoir, Onshore Texas, USA. *Pure and Applied Geophysics*, 174, 4137–4152. <https://doi.org/10.1007/s00024-017-1620-0>.
- Saenger, E. H., & Bohlen, T. (2004). Finite-difference modeling of viscoelastic and anisotropic wave propagation using the rotated staggered grid. *Geophysics*, 69, 583–591. <https://doi.org/10.1190/1.1707078>.
- Saenger, E. H., Kruger, O. S., & Shapiro, S. A. (2006). Effective elastic properties of fractured rocks: Dynamic vs. static considerations. *Int J Fracture*, 139, 569–576. <https://doi.org/10.1007/s10704-006-0105-4>.
- Stewart, R. R., Dyaour, N., Omoboya, B., de Figueiredo, J. J. S., Willis, M., & Sil, S. (2013). Physical modeling of anisotropic domains: Ultrasonic imaging of laser-etched fractures in glass. *Geophysics*, 78, D11–D19. <https://doi.org/10.1190/geo2012-0075.1>.
- Sun, R., McMechan, G. A., Hsiao, H. H., & Chow, J. (2004). Separating P- and S-waves in prestack 3D elastic seismograms using divergence and curl. *Geophysics*, 69, 286–297. <https://doi.org/10.1190/1.1649396>.
- Vlastos, S., Liu, E., Main, I. G., & Li, X. Y. (2003). Numerical simulation of wave propagation in media with discrete distributions of fractures: effects of fracture sizes and spatial distributions. *Geophysical Journal International*, 152, 649–668. <https://doi.org/10.1046/j.1365-246X.2003.01876.x>.
- Wu, Z., Fan, L., & Zhao, S. (2018). Effects of hydraulic gradient, intersecting angle, aperture, and fracture length on the nonlinearity of fluid flow in smooth intersecting fractures: An experimental investigation. *Geofluids*, 2018, 1–14. <https://doi.org/10.1155/2018/9352608>.
- Zazoun, R. S. (2008). The Fadnoun area, Tassili-n-Azdjer, Algeria: Fracture network geometry analysis. *Journal of African Earth Sciences*, 50, 273–285. <https://doi.org/10.1016/j.jafrearsci.2007.10.001>.
- Zhang, R., Vasco, D., & Daley, T. M. (2015). Study of seismic diffractions caused by a fracture zone at In Salah carbon dioxide storage project. *International Journal of Greenhouse Gas Control*, 42, 75–86. <https://doi.org/10.1016/j.ijggc.2015.07.033>.